Check for updates

Advanced Functional Materials

ADVANCED FUNCTIONAL MATERIALS
www.afm-journal.de

RESEARCH ARTICLE

Programmable 3D-Orthotropic Piezoceramic Sensors Enabled by Solid-Loading-Maximized Additive Manufacturing

Peipei Wang[1] | Yaxiang Sun[1] | Wei Zhao[2] | Xin Lan[1] | Yanju Liu[2,3] | Jinsong Leng[1]

[1]Centre for Composite Materials and Structures, Harbin Institute of Technology, Harbin, China | [2]Department of Aerospace Engineering and Mechanics, Harbin Institute of Technology, Harbin, China | [3]Suzhou Research Institute, Harbin Institute of Technology, Suzhou, China

Correspondence: Xin Lan (lanxin@hit.edu.cn) | Yanju Liu (yj_liu@hit.edu.cn)

Received: 9 September 2025 | **Revised:** 27 June 2026 | **Accepted:** 2 July 2026

Keywords: 3d printing | high precision | high solid loading | piezoelectric ceramics | piezoelectric sensors

ABSTRACT

Additive manufacturing has opened new avenues for geometric customization and functional integration of piezoelectric ceramics, yet conventional methods face irreconcilable conflicts between ultrahigh solid-loading and microscale precision, fundamentally limiting their electromechanical performance and structural-sensing fidelity. Here, this work presents a precision 3D printing strategy based on ultrahigh solid loading (90 wt.%), achieving minimal defect $BaTiO_3$ piezoelectric ceramics with synchronized enhancement of functional and mechanical properties through optimized rheological behavior. This approach attains optimized piezoelectric coefficient (d_{33} > 240 pC N^{-1}) and mechanical robustness (compressive strength > 340 MPa), delivering overall performance comparable to conventional dry-pressed ceramics. Simultaneously, the process enables high-resolution fabrication of monolithic devices (<5 mm edge length) incorporating sub-200 μm critical features. Crucially, a general design framework programs 3D-orthotropic sensing into architected triply periodic minimal surface (TPMS) microstructures through parameterized symmetry-breaking. This process converts tailored mechanical anisotropy, combined with a fixed poling direction, into orthogonal sensitivity gradients and structural-signal fidelity. The resulting sensing platforms demonstrate high sensitivity (0.42 V N^{-1}), high linearity (R^2 > 0.999), near-zero delay with waveform synchronism, and power density (>68 μW cm^{-3}), enabling orthotropic force discrimination along three orthogonal axes for autonomous microsystems. This work advances the manufacturing paradigm for high-performance piezoelectric ceramics, offering scalable potential for microsensors and energy harvesters.

1 | Introduction

The pursuit of advanced sensing capabilities in miniaturized systems [1, 2]—from implantable medical devices to micro-robotic end-effectors [3]—has intensified the need for piezoelectric materials that can discriminate mechanical stimuli along orthogonally oriented axes [4, 5]. Such directional sensitivity demands not only high electromechanical conversion efficiency but microarchitectural designs that encode anisotropic response into material fabric [6, 7]. Barium titanate ($BaTiO_3$) ceramics, as premier lead-free piezoelectrics, possess intrinsic advantages including high piezoelectric coefficients, thermal stability, and biocompatibility [8–10]. Yet conventional manufacturing techniques remain fundamentally inadequate [11]: dry pressing [12], slip casting, and tape casting cannot create spatially graded lattice geometries [13–15] or continuous microscale features [16–19] essential for engineered strain localization and orthogonally differentiated signal generation. This incapacity becomes progressively constraining as applications evolve toward systems requiring coordinated geometric programmability and axis-specific responsivity [20, 21].

All rights reserved, including rights for text and data mining and training of artificial intelligence technologies or similar technologies.
© 2026 Wiley-VCH GmbH

Additive manufacturing (AM) promised a paradigm shift by enabling complex geometries through layer-wise fabrication [22–24]. Digital light processing (DLP), in particular, achieves sub-50 μm resolution by photopolymerizing ceramic-filled resins [25–27]. However, its applicability to piezoelectric ceramics remains constrained by a trilemma of high solid loading [28, 29], high forming precision [25], and high electromechanical performance [30], which are interdependent yet mutually conflicting. Achieving ultrahigh solid-loading (>85 wt.%) is critical for maximizing piezoelectric coefficients, yet elevated ceramic content intensifies refractive index contrast between $BaTiO_3$ particles and organic matrices, exacerbating light scattering that degrades curing resolution and interlayer adhesion [31]. Concurrently, maintaining micron-scale precision necessitates homogeneous slurry recoating, but high solid-loading drastically increases viscosity [32], causing non-uniform layer deposition and incomplete crosslinking [33]—especially detrimental to overhanging structures. Furthermore, ensuring electromechanical reliability requires defect-free microstructures post-sintering, yet the compromises between solid-loading [34] and precision invariably introduce pores, cracks, and delamination that erode mechanical integrity and electrical poling efficiency. Current studies typically maintain ceramic loading around 80 wt.% (approximately 40 vol%) [35–37], achieving piezoelectric coefficients of approximately 200 pC N^{-1} [33, 38] and compressive strengths of 250 MPa [39]. While formulations approaching 90 wt.% have been reported, rheological instabilities and defect accumulation often create a performance inflection point around 80 wt.% solid loading [40, 41]. Beyond this threshold, further increases in solid loading typically introduce defects that concurrently diminish dimensional accuracy, electrical properties, and mechanical strength [33, 41]. These process-induced limitations collectively stifle the realization of architecturally programmed sensing anisotropy.

The repercussions for sensing functionality are profound: insufficient solid-loading caps piezoelectric charge constants below 200 pC N^{-1} [33], curbing voltage sensitivity [42]; inadequate printing precision in high-solid-loading systems impedes the fabrication of micro architectures necessary for strain-field manipulation [43, 44], constraining axis-specific signal discrimination; and interfacial defects induce dynamic phase decoherence and waveform distortion that undermine signal stability [45]. Consequently, state-of-the-art AM piezoceramics remain confined to demonstrating basic, lacking both engineered anisotropy for orthotropic sensitivity and synchronized geometric-functional fidelity essential for next-generation sensing [4, 46].

To address these multidimensional challenges, a solid-loading-maximized additive manufacturing strategy for piezoceramics was developed, establishing a comprehensive methodology centered on formulation design and process optimization of photopolymerizable $BaTiO_3$ slurries at 90 wt.% (over 62 vol%) solid-loading. Rigorous rheological characterization was conducted to ensure printability of high-solid-loading systems, followed by synergistic control of solid-loading and sintering temperature to govern microstructure evolution. Integrated electromechanical property assessment was performed to evaluate the overall performance. Complex three-dimensional architectures with continuous micron-scale features were subsequently fabricated to enable systematic evaluation of piezoelectric sensing behavior, particularly focusing on orthotropic signal differentiation capabilities arising from micro-architectural anisotropy. The directional sensitivity characteristics were probed under controlled mechanical stimulation, with signal linearity and dynamic phase coherence quantified to assess sensing fidelity. This systematic investigation deciphers the processing-structure-property interplay in high-loading precision piezoceramics, while validating applicability in functional microsystems requiring coordinated geometric accuracy and electromechanical response stability for advanced sensing implementations.

2 | Results and Discussion

2.1 | Solid-Loading-Maximized Additive Manufacturing

Figure 1a illustrates the high-solid-loading $BaTiO_3$ ceramic slurry with a bimodal particle size distribution (Section S1.1) and its printing process. The viscosity of high-solid-loading $BaTiO_3$ ceramic slurries as a function of shear rate is shown in Figure 1b. Under high shear rate conditions, all ceramic slurries exhibited a decreasing viscosity trend, consistent with typical shear-thinning non-Newtonian fluid behavior. Notably, this behavior was well-preserved even in the 90 wt.% slurry. At high shear rates, the viscosities of 80, 85, and 90 wt.% $BaTiO_3$ ceramic slurries decreased to 0.48, 1.88, and 3.22 Pa·s, respectively. This is consistent with theoretical trends (Section S1.2). The applied shear force disrupted the flocculated structure dominated by van der Waals forces and electrostatic interactions between particles, inducing particle alignment along the shear direction and consequently reducing flow resistance. During blade coating, the high shear rate resulted in lower viscosity, ensuring uniformity of thin layers and improving interlayer adhesion. Meanwhile, the ceramic slurry sedimentation test demonstrates good stability and dispersibility within 7 days (Section S1.3). The pouring process of slurries was recorded to assess their flow behavior with varying solid loadings (Video S1). The high-solid-loading ceramic slurry was subsequently employed for precision printing (Section S1.4), followed by a two-step debinding and sintering process (Section S2.1) to obtain the final dense piezoceramic components.

The linear shrinkage rates of the 80, 85, and 90 wt.% solid-loading ceramics were measured as approximately 21.50%, 15.50%, and 11.00%, as shown in Figure 1c. Importantly, increasing solid loading enhanced the optimal relative density from 92.84 ± 0.22% (80 wt.%) to 93.75 ± 0.24% (90 wt.%), while suppressing linear shrinkage by 48.8%, as shown in Figure 1d. A strong negative correlation (R^2 = 0.993) between solid loading and dimensional shrinkage was statistically confirmed. Additionally, the XRD patterns show that the splitting at 45° intensifies, indicating a gradual enrichment of the tetragonal phase (Section S2.2). Critically, the 90 wt.% high-solid-loading green bodies demonstrated exceptional process robustness by maintaining structural integrity throughout printing, debinding, and sintering, while simultaneously enhancing dimensional stability during densification. This dual advantage is attributed to the reduced binder content, which suppresses pyrolysis-induced porosity and promotes particle rearrangement in the sintering process.

16163028, 2026, 79, Downloaded from https://advanced.onlinelibrary.wiley.com/doi/10.1002/adfm.202523909 by Harbin Institute Of Technology, Wiley Online Library on [12/11/2026]. See the Terms and Conditions (https://onlinelibrary.wiley.com/terms-and-conditions) on Wiley Online Library for rules of use; OA articles are governed by the applicable Creative Commons License

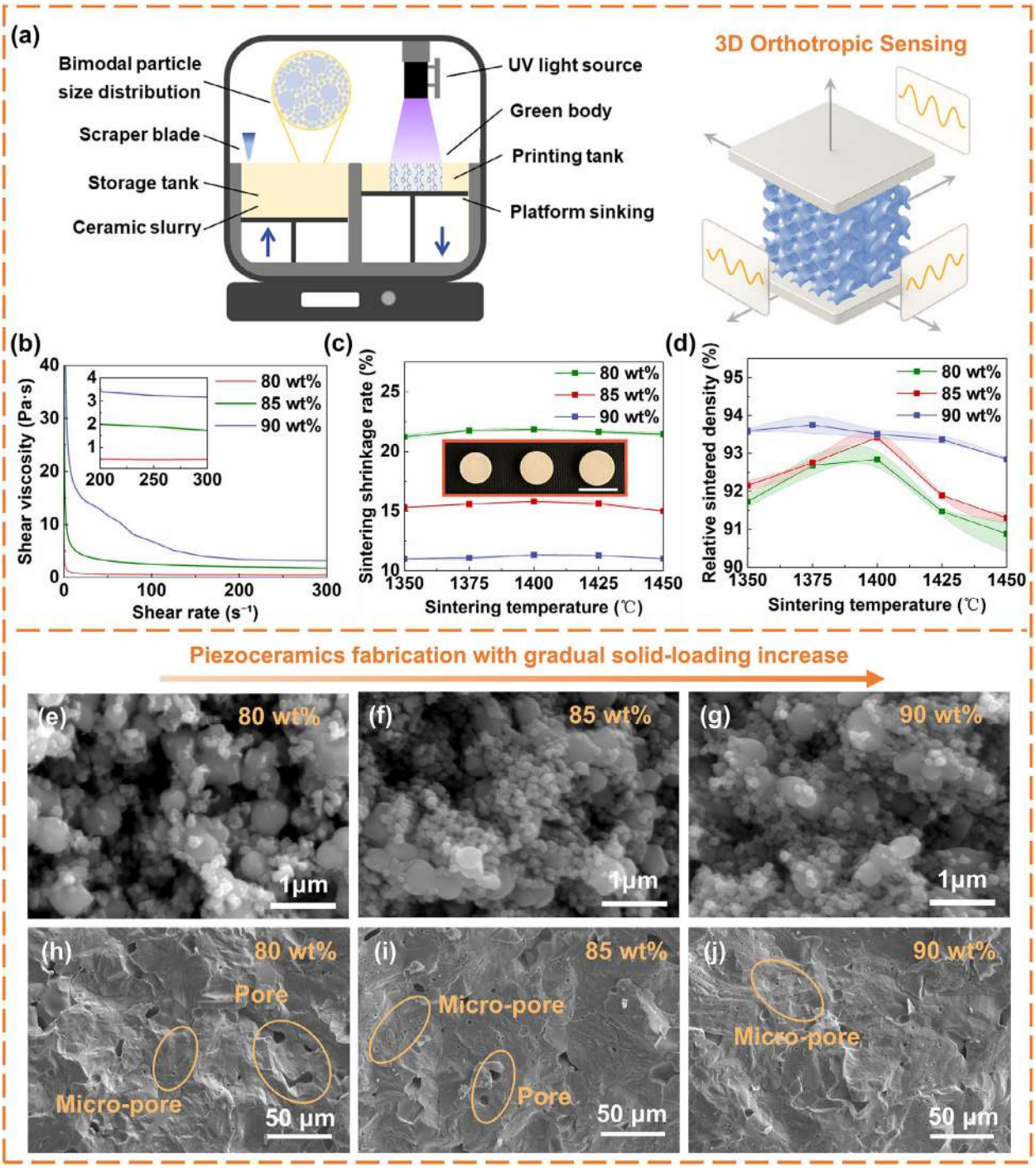


FIGURE 1 | Fabrication and sintering performance of solid-loading-maximized 3D printed piezoceramics. (a) Ceramic slurry with bimodal particle size distribution and printing process. (b) Effect of solid loading on the rheological properties. Variations in (c) sintering shrinkage rate and (d) relative sintered density of piezoelectric ceramics as functions of sintering temperature and solid loading (scale bar: 1 cm) ($n = 3$). SEM images of piezoelectric ceramics after debinding (e–g) and fracture surfaces after sintering (h–j) for solid loadings of 80, 85, and 90 wt.%.

The microstructural evolution of 3D-printed $BaTiO_3$ ceramics with varying solid loadings was systematically analyzed via scanning electron microscopy. Figure 1e–g present cross-sectional SEM images of debinded ceramics, confirming complete resin removal. Increasing solid loading from 80 to 90 wt.% enhanced particle packing, evidenced by reduced interparticle voids. The bimodal particle distribution with a fine-to-coarse ratio of 4 to 6 remained consistent with design targets, facilitating intergranular filling as fine particles occupied the interstitial sites between coarse particles.

As shown in Figure 1h–j, the 80, 85, and 90 wt.% solid-loading ceramics sintered at 1375°C exhibited progressive densification with reduced intergranular voids and defects. Critically, the 90 wt.% ceramic sintered at 1375°C eliminates macropores through optimized particle gradation and diffusion-driven pore

16163028, 2026, 79, Downloaded from https://advanced.onlinelibrary.wiley.com/doi/10.1002/adfm.202523909 by Harbin Institute Of Technology, Wiley Online Library on [12/11/2026]. See the Terms and Conditions (https://onlinelibrary.wiley.com/terms-and-conditions) on Wiley Online Library for rules of use; OA articles are governed by the applicable Creative Commons License

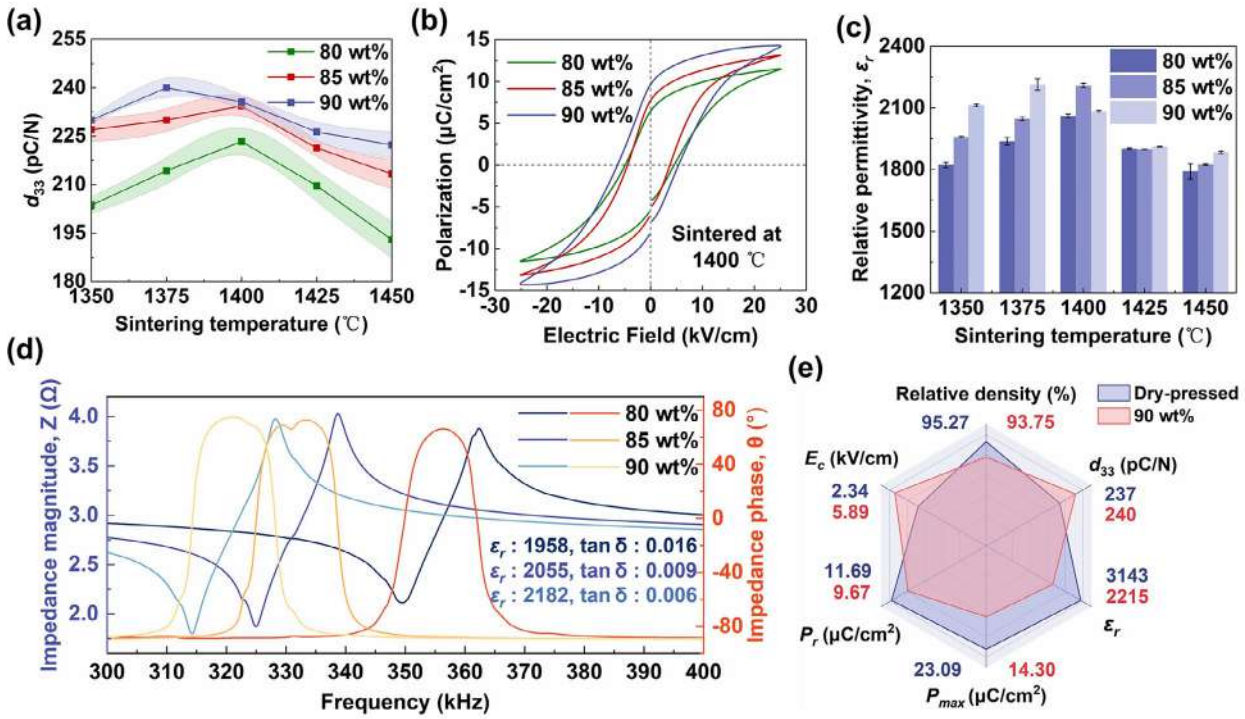


FIGURE 2 | Excellent electrical performance rivaling dry-pressed ceramics. Dependence of (a) piezoelectric coefficient (d_{33}) on sintering temperature and solid loading ($n = 3$). (b) Effect of solid loading on P-E hysteresis loops. (c) Dependence of relative permittivity (ε_r) on sintering temperature and solid loading ($n = 3$). (d) Impedance spectra (1375°C). (e) Performance comparison between 3D-printed (90 wt.%) and dry-pressed $BaTiO_3$ ceramics.

closure. This enables superior compressive strength despite residual micro-porosity from constrained gas evolution and grain-boundary pore pinning, highlighting the essential processing-microstructure-property nexus. Meanwhile, the SEM images of the surfaces of the piezoelectric ceramics are displayed (Section S2.3). Notably, the 90 wt.% ceramics demonstrated pronounced grain coalescence, where larger grains assimilated smaller ones via boundary migration, leading to an increase in average grain size compared to those with lower solid loading. Evident grain growth at elevated temperatures is illustrated (Section S2.4). The high solid loading facilitated effective low-temperature densification by enhancing particle coordination and suppressing porosity, ultimately optimizing both microstructural homogeneity and electromechanical performance.

2.2 | Electromechanical Performance Characterization

The piezoelectricity of $BaTiO_3$ ceramics is governed by 90° domain wall motion, which is hindered by depolarization fields at pore surfaces. 90 wt.% ceramics sintered at 1375°C achieved the highest piezoelectric coefficient d_{33} of 240 ± 3 pC N^{-1}, corresponding to the peak relative density of 93.75%, as shown in Figure 2a. Comparatively, 85 and 80 wt.% ceramics reached d_{33} maxima of 234 ± 3 and 223 ± 4 pC N^{-1} at 1400°C. Increasing solid loading to 90 wt.% enhanced d_{33} by 7.62%, attributed to reduced porosity suppressing depolarization effects. SEM analysis confirmed that the 90 wt.% ceramics exhibited minimal intergranular voids and homogeneous microstructure, thereby enhancing domain wall mobility and optimizing electromechanical coupling.

Figure 2b presents the P-E hysteresis loops of $BaTiO_3$ ceramics with 80, 85, and 90 wt.% solid loadings under 25 kV cm^{-1}. The ceramics sintered at 1375°C and 1400°C exhibited strong ferroelectricity due to high densification and minimal defects (Section S3.1). Increasing solid loading significantly enhanced performance, with the 90 wt.% ceramic achieving a maximum polarization P_{MAX} of 14.30 μC cm^{-2}, a remnant polarization P_r of 9.67 μC cm^{-2}, and a coercive field E_C of 5.89 kV cm^{-1}. These values represent improvements of 24.35%, 49.23%, and 24.79%, respectively, compared to the 80 wt.% ceramic. This enhancement was attributed to the reduced porosity, which lowered the depolarization field and promoted uniform electric field distribution in the ceramic. The dense microstructure with high density and low porosity resulted in an increased coercive field, reflecting enhanced domain switching energy, and indicated better stability under high electric fields.

The relative permittivity (ε_r) and dielectric loss ($tan\,\delta$) of 3D-printed $BaTiO_3$ ceramics were characterized via impedance analysis at 1 kHz. The 90 wt.% ceramic sintered at 1375°C exhibited the highest relative permittivity of 2215 ± 27, while 85 and 80 wt.% ceramics achieved ε_r maxima of 2209 ± 11 and 2061 ± 9 at 1400°C, respectively, as shown in Figure 2c. Increasing solid loading from 80 to 90 wt.% enhanced ε_r by 7.47%, which is attributed to improved polarization stemming from facilitated 90° domain wall motion under an external field. Conversely, depolarization fields at pore surfaces restricted domain mobility, thereby suppressing permittivity in the lower-density ceramics.

Concurrently, ε_r values for 80, 85, and 90 wt.% ceramics sintered at 1375°C were 1958, 2055, and 2182, respectively, with corresponding

16163028, 2026, 79, Downloaded from https://advanced.onlinelibrary.wiley.com/doi/10.1002/adfm.202523909 by Harbin Institute Of Technology, Wiley Online Library on [12/11/2026]. See the Terms and Conditions (https://onlinelibrary.wiley.com/terms-and-conditions) on Wiley Online Library for rules of use; OA articles are governed by the applicable Creative Commons License

$tan\,\delta$ values of 0.016, 0.009, and an exceptionally low value of 0.006, as shown in Figure 2d. As the solid loading increased, the Δf bandwidth between the resonance and anti-resonance frequencies widened, indicating that the densified microstructure reduced defects and porosity within the material, thereby enhancing its electromechanical coupling performance.

Furthermore, a direct performance benchmark was established by fabricating ceramic pellets via dry pressing using the identical bimodal powder mixture (Section S3.3). A radar chart comparing key properties of the 90 wt.% 3D-printed ceramic and the dry-pressed counterpart are presented in Figure 2e. It demonstrates that the overall functional performance, particularly the piezoelectric coefficient, of the 3D-printed ceramic is comparable to that of the conventionally fabricated standard, while additionally granting the freedom of architectural design.

The mechanical properties of 3D-printed $BaTiO_3$ ceramics, including elastic modulus E^* and hardness H, were evaluated via micro/nanoindentation. For 85 wt.% ceramics sintered at temperatures ranging from 1350°C to 1450°C, E^* and H initially increased with temperature, peaking at 171 ± 6 GPa and 6111 ± 110 MPa at 1400°C, followed by a decline at higher temperatures, as shown in Figure 3a. This trend confirms 1400°C as the optimal sintering temperature for 85 wt.% ceramics, which balances interparticle bonding strength and avoiding oversintering-induced microcracks or abnormal grain growth. At 1400°C, E^* values for 80, 85, and 90 wt.% ceramics were 149 ± 22, 171 ± 6, and 177 ± 22 GPa, respectively, representing an 18.79% improvement for 90 wt.% over 80 wt.%, as shown in Figure 3b. However, the 90 wt.% ceramic exhibited a slight reduction in H compared to 85 wt.%, due to oversintering effects at 1400°C, as its optimal sintering temperature was identified at 1375°C. The corresponding load–unloading curves are displayed (Section S3.2).

The compressive strength of $BaTiO_3$ ceramics with varying solid loadings and sintering temperatures was systematically investigated, as shown in Figure 3d. Stress–strain curves of the sintered ceramics are shown in Figure 3e. The 90 wt.% ceramic sintered at 1375°C exhibited the highest compressive strength of 342 ± 6 MPa, surpassing the 80 and 85 wt.% counterparts, achieving 327 ± 7 MPa and 334 ± 5 MPa at 1400°C by 4.59% and 2.34%, respectively. This value also significantly exceeds the approximately 250 MPa of $BaTiO_3$ ceramics prepared by DLP that has been reported [39]. The increased compressive strength stems from synergistic effects of enhanced densification, suppressed porosity and controlled grain growth, which collectively minimize stress-concentration defects while optimizing load-bearing pathways. The compressive strength reaches its peak at the optimal sintering temperature, attributed to the enhanced bonding between particles. However, excessively high temperatures can lead to mechanical degradation due to excessive grain growth and potential phase transformations. This underscores the necessity of tailoring the sintering temperature for high-solid-loading formulations to ensure microstructural stability and mechanical integrity.

This work achieves micrometer-level precision forming of ceramic slurries with ultrahigh solid loading, surpassing the electrical performance and mechanical strength of previously reported 3D-printed $BaTiO_3$ ceramics. Existing studies primarily focus on solid loading between 70 and 85 wt.%, with a notable inflection point around 80 wt.% due to rheological instabilities and defect accumulation, as shown in Figure 3c. In contrast, the high-solid-load slurries optimized in this research eliminate these inflection points, delivering continuous enhancements in piezoelectric and dielectric properties across 80–90 wt.% without performance saturation. Crucially addressing a critical knowledge gap, it establishes performance optimization protocols for 85–90 wt.% solid-loading slurries, a previously unexplored regime.

The $BaTiO_3$ ceramics with high solid loading exhibit exceptional comprehensive electrical properties, including piezoelectric and dielectric performance, surpassing previously reported findings, as shown in Figure 3f. Remarkably, demonstrating concurrent high precision and performance, these high solid-loading piezoceramics redefine attainable property limits, as shown in Figure 3h. Specifically, the 90 wt.% $BaTiO_3$ ceramic exhibits a characteristic size as fine as 182 μm, a piezoelectric coefficient d_{33} of 240 pC N^{-1}, and a compressive strength of 342 MPa, significantly outperforming existing literature. This highlights the remarkable advantages of high solid loading formulations in enhancing electro-mechanical properties.

The breakthrough "Triple-High" synergy (high solid loading, high precision, and high performance) is quantifiably demonstrated via multi-property radar analysis, as shown in Figure 3g. The figure highlights a systematic comparison of ceramics with varying solid loading, with the 90 wt.% ceramic exhibiting outstanding comprehensive properties. These include exceptional electrical performance, characterized by superior piezoelectric, dielectric, and ferroelectric characteristics, along with excellent mechanical performance, marked by compressive strength and elastic modulus. Additionally, the ceramic demonstrates outstanding sintering quality, with minimal shrinkage rate and high relative density, while achieving remarkable micron-level forming precision. This groundbreaking achievement holds significant implications for advancing the development of high-loading, high-performance, and high-precision functional ceramic components.

This work demonstrates the precise printing of complex architectures in piezoelectric ceramics using DLP-based 3D printing, achieving exceptional microscale structural fidelity while maintaining high performance. As shown in Figure 4a, all solid loadings successfully printed 100 μm thin-wall structures, while microcolumn resolution varies. Specifically, 80 wt.% attains 150 μm columns with partial collapse at 100 μm, whereas 85 and 90 wt.% achieve 200 μm columns with partial success at 150 μm. Furthermore, triply periodic minimal surface (TPMS) structures (Primitive, I-WP, Gyroid) and body-centered cubic (BCC) lattices are flawlessly printed and sintered, with unit cell sizes of 2 mm (TPMS) and 1.5 mm (BCC), as shown in Figure 4b–e.

SEM images reveal that the sintered ceramic structures exhibit excellent structural integrity, with feature sizes ranging from 110 to 334 μm, as shown in Figure 4f–k. Notably, 80 wt.% ceramics exhibited superior dimensional fidelity, achieving Gyroid structures with minimum wall thicknesses of 122 ± 7 μm,

16163028, 2026, 79, Downloaded from https://advanced.onlinelibrary.wiley.com/doi/10.1002/adfm.202523909 by Harbin Institute Of Technology, Wiley Online Library on [12/11/2026]. See the Terms and Conditions (https://onlinelibrary.wiley.com/terms-and-conditions) on Wiley Online Library for rules of use; OA articles are governed by the applicable Creative Commons License

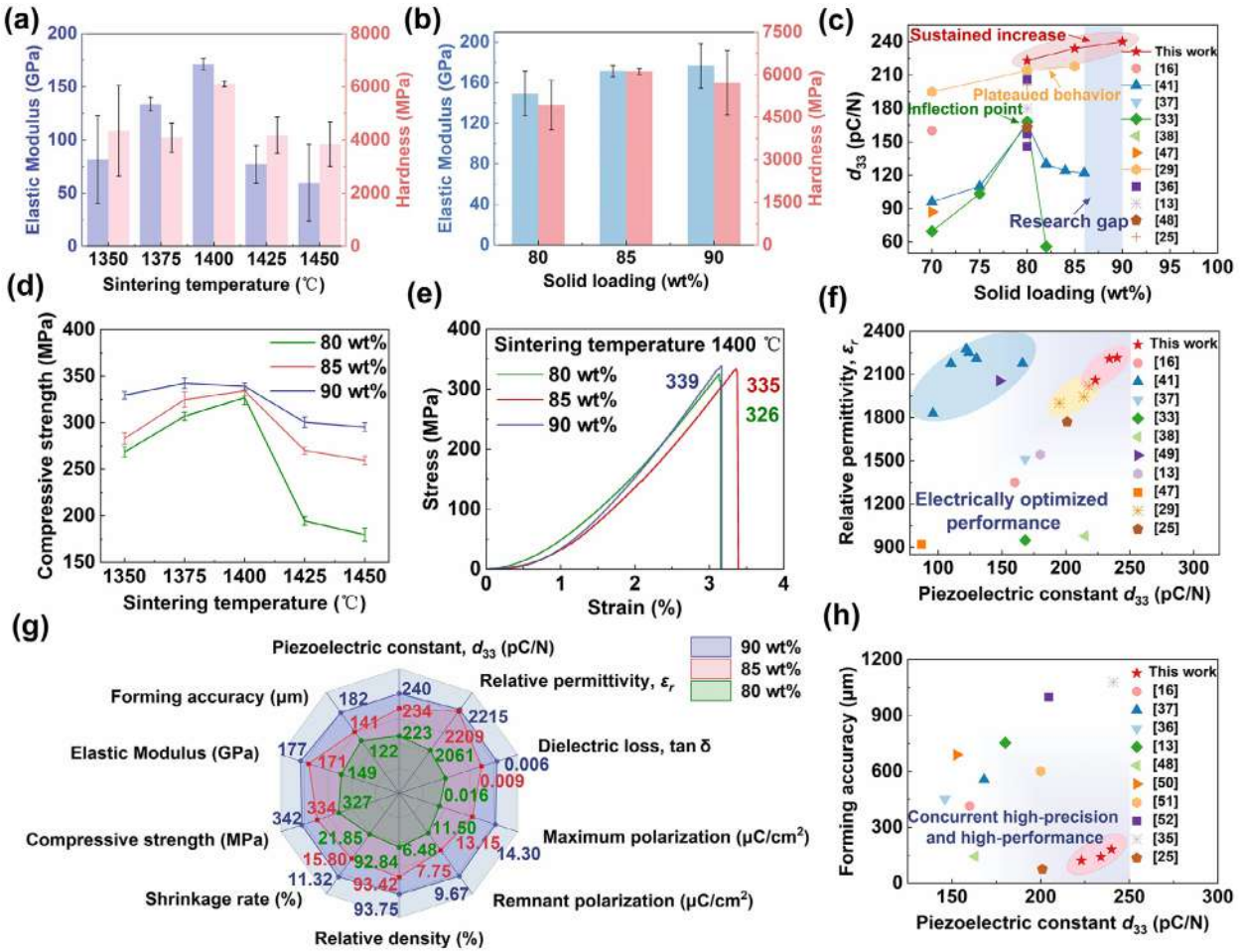


FIGURE 3 | High strength and reliability for structural applications. Nanoindentation elastic modulus and hardness dependence on (a) sintering temperature and (b) solid loading ($n = 3$). (c) Comparison of piezoelectric coefficients of high solid loading piezoelectric ceramics with values reported in the literature [13, 16, 25, 29, 33, 36–38, 41, 47, 48]. (d) Compressive strength evolution with sintering temperature and solid loading ($n = 3$). (e) Representative compressive stress–strain curves. (f) Comparison of piezoelectric coefficients and dielectric constants with those reported in previous works [13, 16, 25, 29, 33, 37, 38, 41, 47, 49]. (g) Multi-attribute performance radar plot. (h) Piezoelectric coefficient and forming accuracy relative to literature [13, 16, 25, 35–37, 48, 50–52].

compared to 141 ± 3 μm for 85 wt.% and 182 ± 6 μm for 90 wt.% (Section S3.4). This difference is attributed to the higher shrinkage rate of 80 wt.% ceramics (~21.50%) compared to 90 wt.% (~11.00%), and the ultrahigh loading of ceramics intensifies light scattering. SEM images of the sintered ceramics demonstrate the successful fabrication of complex structures with preserved geometrical integrity and validate the compatibility of high solid loading with precise microscale geometric control.

2.3 | Axial Piezoelectric Sensing and Energy Harvesting

The piezoelectric voltage constant (g_{33}) and the figure of merit (FOM_{off}) are essential parameters for evaluating the electromechanical conversion efficiency of piezoelectric materials, which can be expressed by the following equations:

$$g_{33} = \frac{d_{33}}{\varepsilon_r \varepsilon_0} \tag{1}$$

$$FOM_{off} = \frac{d_{33} \times g_{33}}{tan\ \delta} \tag{2}$$

The vacuum permittivity ε_0 is $8.854187817 \times 10^{-12}$ F m^{-1}. Sintered piezoelectric ceramics with varying solid loadings exhibit distinct electrical properties and electromechanical conversion performances, as shown in Figure 5a. For ceramics with 80 and 90 wt.%, the g_{33} is 1.23×10^{-2} Vm N^{-1}, while the 85 wt.% ceramic exhibits a slightly lower value due to its relatively higher dielectric constant. Notably, the FOM_{off} for 90 wt.% ceramic reaches as high as $4.90 \pm 0.13 \times 10^{-10}$ m^2 N^{-1}, exceeding typical values [13]. This indicates that 3D-printed $BaTiO_3$ piezoceramics hold substantial promise for high-performance piezoelectric components.

To evaluate the piezoelectric sensing performance, the Gyroid-structured piezoelectric ceramics were cast with epoxy resin and polarized (Section S4.1). For the axial sensing and energy harvesting characterization in this section, the electrodes were connected in a reversed configuration to present the voltage outputs with positive polarity for clarity and intuitive interpretation of the compressive stimuli. A periodic loading

16163028, 2026, 79, Downloaded from https://advanced.onlinelibrary.wiley.com/doi/10.1002/adfm.202523909 by Harbin Institute Of Technology, Wiley Online Library on [12/11/2026]. See the Terms and Conditions (https://onlinelibrary.wiley.com/terms-and-conditions) on Wiley Online Library for rules of use; OA articles are governed by the applicable Creative Commons License

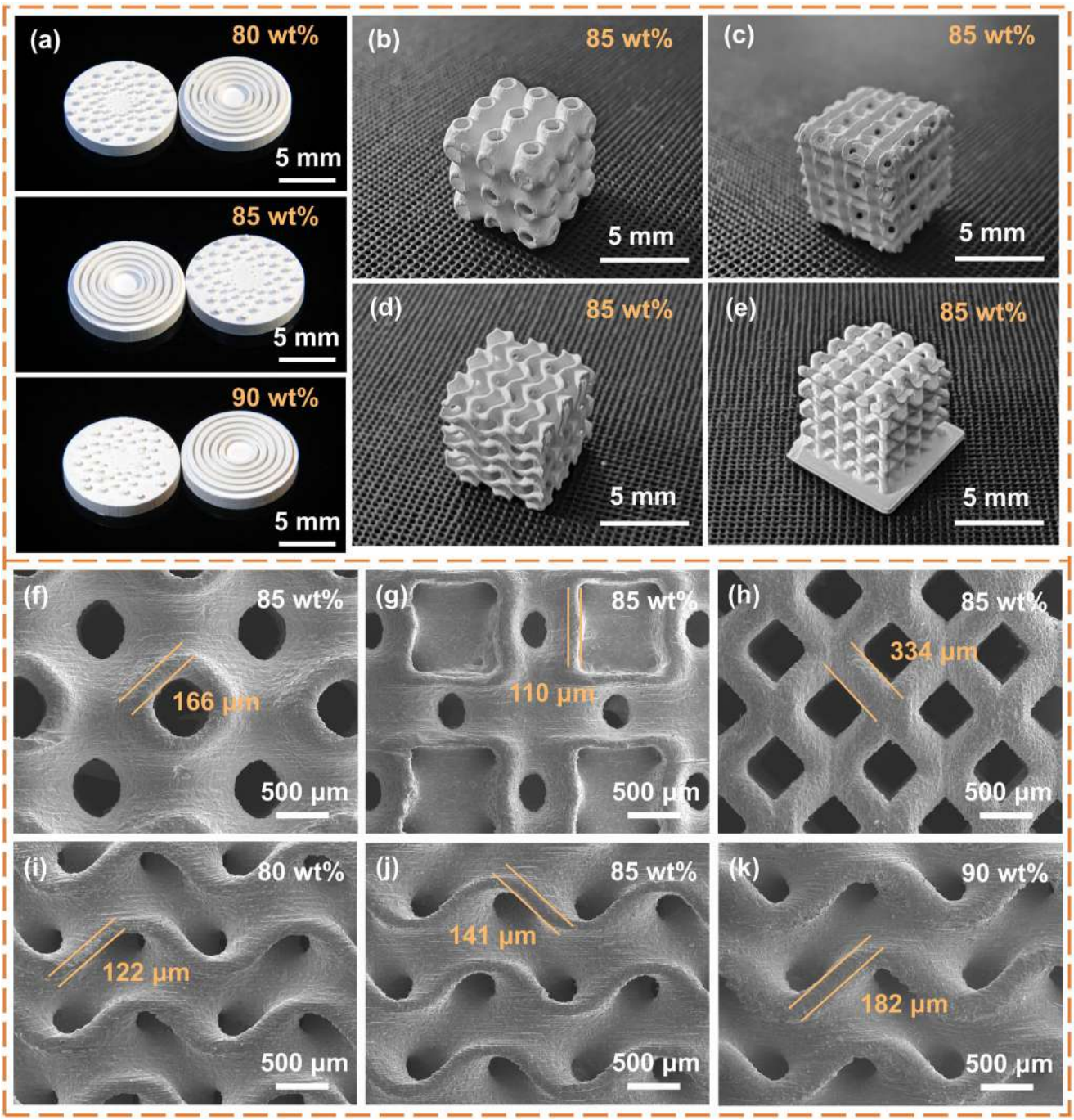


FIGURE 4 | Microfabrication of high-precision piezoceramic sensors. (a) Accuracy testing of thin-wall and micro-column forming under different solid loadings. High-precision 3D continuous microstructure printing of (b) Primitive, (c) I-WP, (d) Gyroid, and (e) BCC structures. SEM images of the corresponding sintered structures. (f) Primitive, (g) I-WP, (h) BCC structures with 85 wt.% solid loading. Comparison of Gyroid structures with (i) 80 wt.%, (j) 85 wt.%, and (k) 90 wt.% solid loadings.

force was generated by a signal generator, charge amplifier, and shaker. The open-circuit voltage response was recorded by an electrometer and data acquisition system to characterize the force-to-electric conversion capability of the ceramic structure. A periodic load of approximately 5 N applied to the 80 wt.% piezoelectric composite induced an alternating piezoelectric voltage of about 0.56 V. The output waveform exhibits a minor DC offset from 0 V, attributable to the inherent characteristics of the testing system. The voltage output exhibited instantaneous temporal synchronism and precise waveform fidelity with the applied mechanical load, confirming robust electromechanical coupling, as shown in Figure 5c,d. Under cyclic loading at 10 Hz, both mechanical and electrical signals achieved synchronous response within 1.4 ms, with virtually undetectable delay. Benchmarking against prior works demonstrates that these response characteristics are remarkably competitive with various types of reported tactile sensors, including piezoelectric, capacitive, resistive, and triboelectric devices, as shown in Figure 5b. The

16163028, 2026, 79, Downloaded from https://advanced.onlinelibrary.wiley.com/doi/10.1002/adfm.202523909 by Harbin Institute Of Technology, Wiley Online Library on [12/11/2026]. See the Terms and Conditions (https://onlinelibrary.wiley.com/terms-and-conditions) on Wiley Online Library for rules of use; OA articles are governed by the applicable Creative Commons License

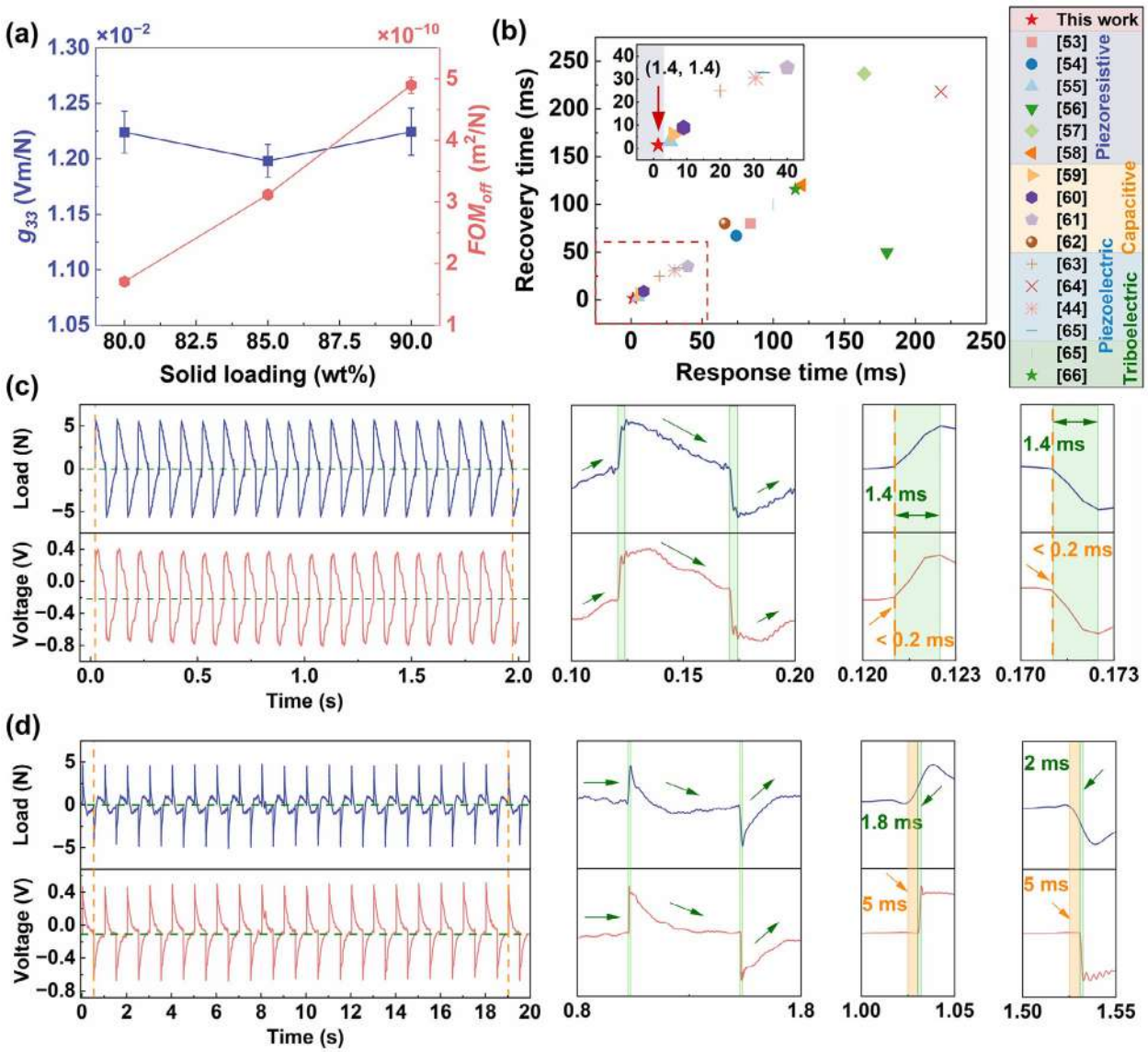


FIGURE 5 | Fast dynamic response of piezoceramic sensors. (a) g_{33} and FOM_{off} with different solid loadings ($n = 3$). (b) Comparison of response and recovery times with prior works [44, 53–66]. (c) Output voltage under 10 Hz loading force. (d) Output voltage under 1 Hz loading force.

system was deployed as a wireless piezoelectric sensor for real-time gait analysis. It successfully captured and distinguished various gait patterns from static to dynamic conditions (Video S2 and Section S4.2).

The piezoceramic sensor integrates both energy harvesting and high-accuracy sensing capabilities, as shown in Figure 6a. Impact testing was performed on an 80 wt.% composite sensor driven by a linear motor stage under periodic impulse loading (40 N, 1 Hz). Current and voltage outputs across varying resistive loads were measured. Power density was determined, revealing a maximum value of 68.60 μW cm^{-3} at 8 MΩ, significantly surpassing previously reported energy harvesting efficiencies, as shown in Figure 6b,c. This result substantiates the promising energy harvesting capabilities of the engineered composite architecture.

Impact testing was performed on the 80 wt.% solid-loading piezoelectric composite under varied forces at 1 Hz. The structure demonstrated a voltage sensitivity of 0.42 V N^{-1} with exceptional force-voltage linearity ($R^2 = 0.99977$), while generating a current of approximately 3 μA under an 80 N load, as shown in Figure 6d–f. Frequency-dependent sensing tests at 60 N loading confirmed that current outputs exhibit significantly stronger frequency sensitivity than voltage signals, as shown in Figure 6g,h. This behavior originates from the linear dependence of piezoelectric current on frequency ($I \propto f$), whereas the voltage output exhibits a much weaker frequency dependence under open-circuit conditions. Cyclic stability testing (60 N, 1 Hz) confirmed consistent voltage and current outputs despite slight intermittent force fluctuations, as illustrated in Figure 6i,l. The 90 wt.% solid-loading variant exhibited lower sensitivity than the 80 wt.% sample, primarily due to compromised charge collection efficiency from increased wall thickness, outweighing the d_{33} enhancement, as illustrated in Figure 6j,k (Section S3.4). These results validate exceptional electromechanical conversion efficiency in 3D-printed piezoceramics, highlighting their promise for high-fidelity sensing applications.

16163028, 2026, 79, Downloaded from https://advanced.onlinelibrary.wiley.com/doi/10.1002/adfm.202523909 by Harbin Institute Of Technology, Wiley Online Library on [12/11/2026]. See the Terms and Conditions (https://onlinelibrary.wiley.com/terms-and-conditions) on Wiley Online Library for rules of use; OA articles are governed by the applicable Creative Commons License

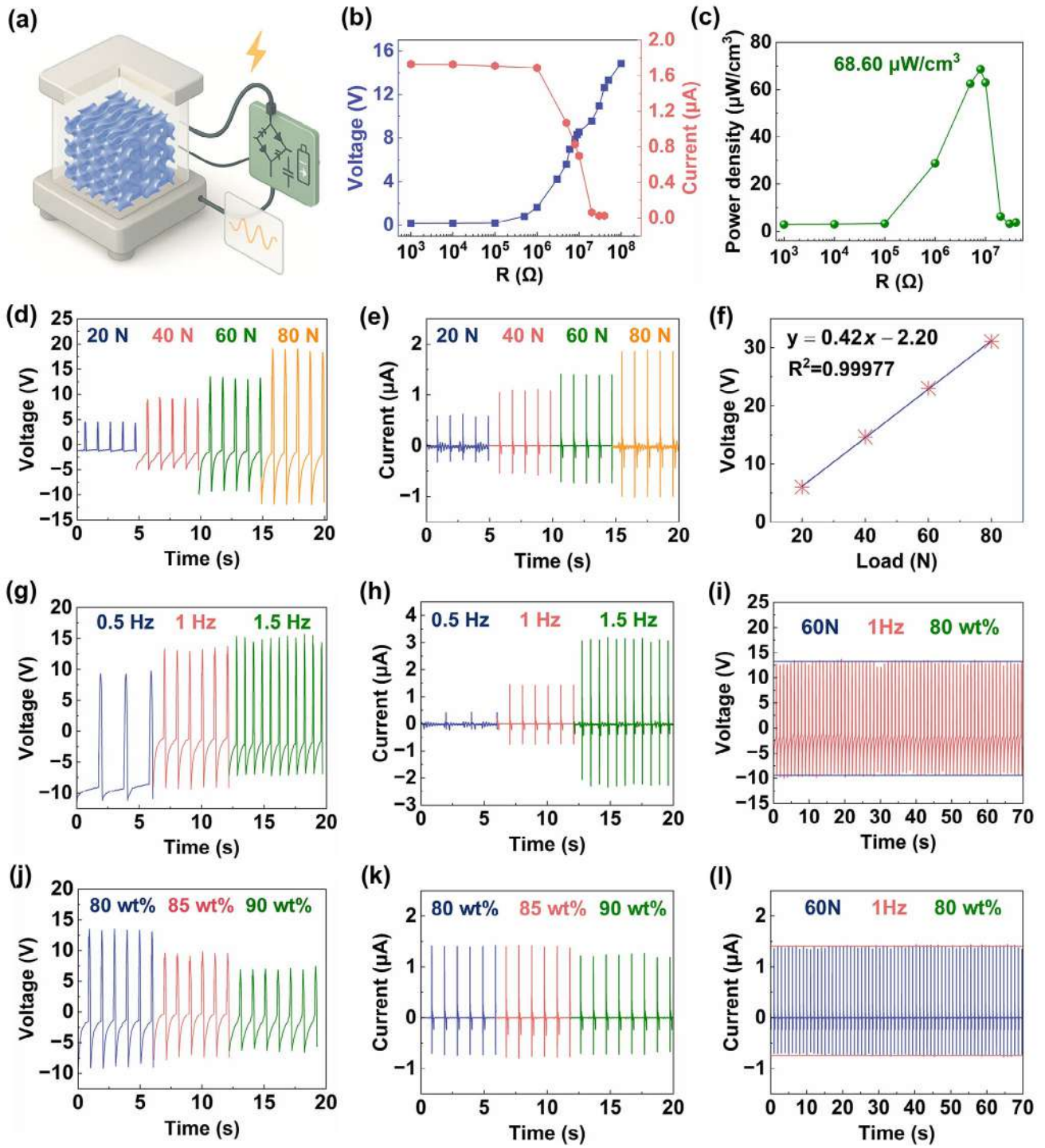


FIGURE 6 | Multifunctional piezoceramic sensors for energy harvesting and high-accuracy sensing. (a) Schematic diagram of the functional integration of piezoelectric sensors. (b) Current, voltage, and (c) power density under different resistance values. (d) Voltage, (e) Current, and (f) linear fitting results under different load forces. (g) Voltage and (h) current values at different frequencies. (i) Cycling stability of output voltage. (j) Voltage and (k) Current under different solid loadings. (l) Cycling stability of output current.

2.4 | 3D Orthotropic Piezoelectric Sensing

Conventional multi-axial force detection requires integrating multiple discrete sensors along different axes. This study presents a paradigm-shifting approach where a single, architectured piezoceramic achieves 3D orthotropic sensing through programmed microstructural design. The methodology establishes a comprehensive "structure-mechanics-sensing" design framework that enables predictable directional force discrimination in monolithic devices.

The framework programs 3D orthotropic sensing by designing geometric anisotropy into TPMS architectures (including Primitive, Gyroid, I-WP, and BCC-like architectures). These are

16163028, 2026, 79, Downloaded from https://advanced.onlinelibrary.wiley.com/doi/10.1002/adfm.202523909 by Harbin Institute Of Technology, Wiley Online Library on [12/11/2026]. See the Terms and Conditions (https://onlinelibrary.wiley.com/terms-and-conditions) on Wiley Online Library for rules of use; OA articles are governed by the applicable Creative Commons License

controlled through three independent scaling parameters (*a, b, c*) that govern spatial periodicity along the *X*, *Y*, and *Z* axes, respectively. Symmetry is broken hierarchically, from isotropic ($a = b = c$) to uniaxially anisotropic (e.g., $a = b \neq c$) and finally to fully orthotropic ($a \neq b \neq c$). This programmed geometric anisotropy dictates the mechanical response, which is subsequently transduced into directional sensing anisotropy under a fixed electrical poling direction (*Z*-axis) (Section S5.1). Crucially, the dimensionality of the resulting sensing anisotropy can exceed that of the mechanical input. For example, a structure with uniaxial mechanical anisotropy can exhibit 3D orthotropic sensing, as stresses from different directions couple to the polarization axis with distinct efficiencies. The Gyroid structure is particularly unique in this context. Its triple-helical and chiral geometry provides an inherent directionality, which introduces an additional "geometric degree of freedom" that significantly enhances the programmability of the sensing anisotropy (Section S5.2). The underlying mathematical framework, which embeds these scaling parameters into implicit equations to modulate distinct topological features, is systematically formulated (Section S5.3).

A unified naming convention (*m, n, l*) is adopted, where $m = 3a/\pi$, $n = 3b/\pi$, and $l = 3c/\pi$ represent relative unit cell densities along *X*, *Y*, and *Z* directions for fixed global dimensions. Numerical homogenization predicts the mechanical anisotropy of various architectures (Section S5.4), while multiphysics simulations coupling Solid Mechanics and Electrostatics modules analyze their piezoelectric responses (Section S5.5). Computational results demonstrate that precise parameter control enables programmable sensing performance ranging from uniaxial to fully 3D orthotropic characteristics.

Fabricated piezoelectric devices based on Primitive and Gyroid structures with systematic parameter variations were prepared, as shown in Figure 7a. To directly reveal the intrinsic anisotropic sensing polarity programmed into the architectures, all devices here were characterized under the standard electrode configuration. The fundamental piezoelectric origin of the measured signals and the systematic effect of electrode configuration were further confirmed by electrode reversal tests (Section S5.6). The isotropic structure (3,3,3) exhibited characteristic uniaxial sensing, while the structure with engineered in-plane anisotropy (2,3,3) successfully broke X-Y sensing symmetry. The fully orthotropic structure (2,3,4) further demonstrated independent sensitivity tuning along all three principal axes. The programmed Gyroid structures with varying parameter codes demonstrate diverse sensing anisotropy, as presented in Figure 7b. The programmed anisotropy across structural, mechanical, and sensing domains is systematically compared, revealing a consistent transformation from geometric design to functional performance (Figure 7c and Section S5.5). The Primitive structure serves as a paradigm for the predictable programming of sensing anisotropy, while the Gyroid exemplifies how architectural complexity can be harnessed to achieve superior and unique sensing capabilities.

This work establishes a fundamental advancement in piezoelectric sensing by transitioning from conventional material selection to architectural programming. The approach of encoding directional sensitivity directly into ceramic micro-architectures overcomes the spatial constraints and integration challenges of multi-sensor arrays, creating a new paradigm where the material structure itself functions as a complete sensing system. This architectural strategy enables single-component discrimination of forces along three orthogonal axes through designed anisotropy, eliminating the need for discrete sensor assemblies.

This programmable 3D orthotropic sensing enables advanced applications in which conventional sensing modalities face limitations, as shown in Figure 7d. For autonomous micro-systems operating in vision-denied environments such as debris fields or confined pipelines, this technology provides essential spatial awareness through directional force discrimination during physical contact. In micro-drone applications, it enables interaction-aware behaviors by distinguishing between collision types and impact directions, supporting appropriate response maneuvers. The monolithic design further facilitates direct integration as both a structural element and a sensing unit in compact systems, maintaining robust performance across challenging operational environments while simplifying system architecture.

3 | Conclusions

In summary, this work establishes a solid-loading-maximized stereolithography strategy that successfully reconciles the long-standing trade-off between ultrahigh solid loading (90 wt.%) and micron-scale precision (<200 μm) in piezoceramic additive manufacturing. Fabricated using a rheologically optimized $BaTiO_3$ slurry, the micro-architected ceramics exhibit superior electromechanical properties, including a piezoelectric coefficient over 240 pC N^{-1} and compressive strength exceeding 340 MPa, matching the performance of conventional dry-pressed ceramics. The micro-architectures demonstrate designed 3D orthotropic sensing with well-defined anisotropic sensitivity and maintain structural–signal fidelity with high linearity ($R^2 > 0.999$) under dynamic loads ranging from 20 to 80 N. Furthermore, the sensors operate with high sensitivity (0.42 V N^{-1}), fast dynamic response, near-zero latency, and power densities greater than 68 μW cm^{-3}. Implemented as a wireless sensor for real-time gait analysis, the system reliably captures both static and dynamic motion signatures, confirming its potential for wearable health monitoring. By unifying ultrahigh-loading precision fabrication, architectured anisotropy, and cross-domain fidelity, this approach shifts the design paradigm from material-oriented optimization to performance-driven micro-architecture engineering. It offers a scalable platform for intelligent systems such as autonomous sensors with multidimensional force resolution, multi-axis energy harvesting platforms, and adaptive human–machine interfaces.

4 | Experimental Section

4.1 | Raw Materials

The raw materials included two distinct fractions of $BaTiO_3$ powder (Macklin, China), namely fine particles (d_{50} = 104.40 nm) and coarse particles (d_{50} = 504.10 nm), both with a density of 6.08 g cm^{-3} (Section S1.1). A photocurable resin (Shenzhen Adventure Tech. Co., Ltd., China) enabled DLP fabrication. For powder surface modification, the additives included Triton X-100 (Macklin, China) as a surfactant, BYK-111 (BYK-Chemie,

16163028, 2026, 79, Downloaded from https://advanced.onlinelibrary.wiley.com/doi/10.1002/adfm.202523909 by Harbin Institute Of Technology, Wiley Online Library on [12/11/2026]. See the Terms and Conditions (https://onlinelibrary.wiley.com/terms-and-conditions) on Wiley Online Library for rules of use; OA articles are governed by the applicable Creative Commons License

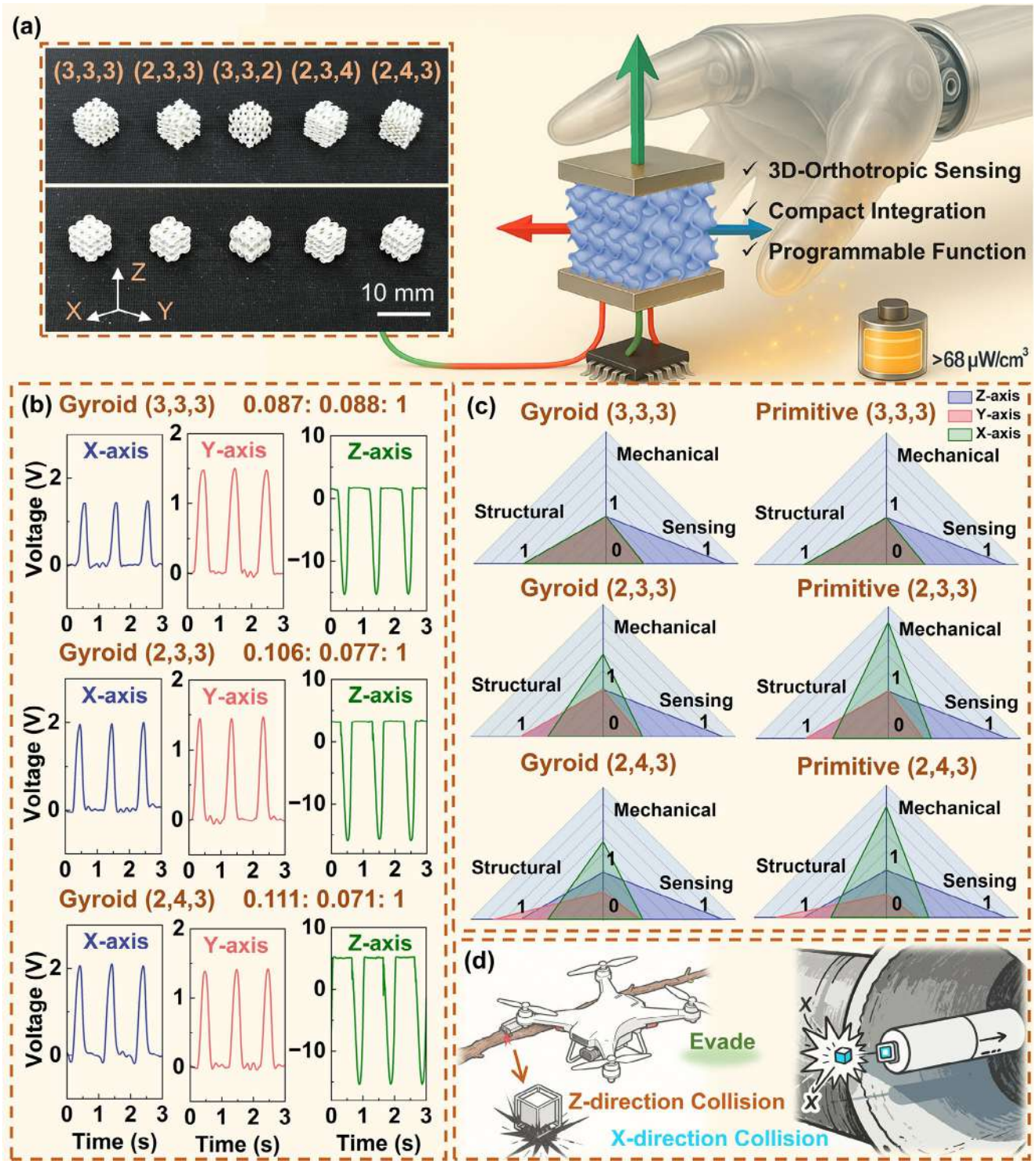


FIGURE 7 | Orthotropic sensing performance of piezoceramic sensors. (a) Parametrically programmed piezoelectric ceramic architectures (green bodies). (b) Anisotropic sensing responses of differently encoded Gyroid structures. (c) Comparison of anisotropy across structural, mechanical, and sensing domains (all values normalized to the *Z*-axis value of 1). (d) Application prospects in autonomous micro-systems and micro-drones, enabled by monolithic integration.

Germany) as a dispersant, and 4-Methoxyphenol (MEHQ, Macklin, China) as a polymerization inhibitor. Additionally, phenyl bis(2,4,6-trimethylbenzoyl)-phosphine oxide (XBPO, Macklin, China) served as a photoinitiator, while tetraethyl orthosilicate (TEOS, Macklin, China) acted as a sintering aid.

4.2 | Slurry Preparation

$BaTiO_3$ ceramic powders were mixed into the slurry at solid loadings of 80, 85, and 90 wt.%, with a mass ratio of fine to coarse particles of 4:6. Based on our previous work [67], this

16163028, 2026, 79, Downloaded from https://advanced.onlinelibrary.wiley.com/doi/10.1002/adfm.202523909 by Harbin Institute Of Technology, Wiley Online Library on [12/11/2026]. See the Terms and Conditions (https://onlinelibrary.wiley.com/terms-and-conditions) on Wiley Online Library for rules of use; OA articles are governed by the applicable Creative Commons License

bimodal particle size distribution facilitates optimal packing density and sintering density of the ceramics, while simultaneously improving the rheological properties of the slurry. Surfactant and dispersant were added at 2 and 1 wt.% of the $BaTiO_3$ powder mass, respectively. The mass ratio of photopolymer resin, polymerization inhibitor, and photoinitiator was fixed at 100:0.5:2. Additionally, a sintering aid was introduced at 2 wt.% based on the total slurry mass.

The slurry was prepared by first mixing all components except the ceramic powders for 30 min to form a pre-mix. Ceramic powders were added and subjected to ball milling at 800 r min^{-1} for 2 h, 400 r min^{-1} for 2 h, and 200 r min^{-1} for 4 h. The slurry was then vacuum defoamed at 10 kPa for 10 min, yielding a stable slurry with a bimodal particle size distribution and varying solid loadings.

4.3 | DLP 3D Printing Process

The ceramic green bodies were fabricated using a high-precision dual-vat sinking-type DLP 3D printer (ADT-3D-ZP-Printer-96-50, Shenzhen Adventure Tech. Co., Ltd., China) (Section S1.4). Key printing parameters included a layer thickness of 30 μm, UV exposure time of 5 s, power density of 58 mW cm^{-2}, and a wavelength of 405 nm.

4.4 | Debinding and Sintering Processes

A two-step debinding process in argon and air atmospheres, followed by high-temperature sintering in air, was employed (Section S2.1). The ceramic green bodies were heated stepwise in argon to 120°C, 240°C, 385°C, and 500°C, holding at each stage to ensure complete carbonization of the organics. Subsequently, oxidation and decarbonization were carried out in air by staged heating to 120°C, 425°C, and 500°C with holding periods at each temperature. Finally, the sintering process was performed in air by heating at a rate of 2°C min^{-1} to the sintering temperature, followed by a 2 h dwell to promote densification of the ceramic.

4.5 | Material Characterization

The shear viscosity of the ceramic slurry was characterized using a rotational rheometer (Kinexus Lab+, NETZSCH, Germany). The phase composition of the sintered piezoelectric ceramics was analyzed using an X-ray diffractometer (XRD, X'PERT, Panalytical, Netherlands). The density of the sintered piezoelectric ceramics was measured by the Archimedes drainage method. The shrinkage rate of the piezoelectric ceramics was calculated by comparing the dimensions of the sintered and green bodies. The morphology of $BaTiO_3$ ceramic powder, as well as the microstructures of the debinded body, sintered body, and fracture surface, were observed using a scanning electron microscope (SU5000, Hitachi High-Tech, Japan).

Prior to electrical performance testing, silver electrodes were coated on the top and bottom surfaces of the sintered piezoelectric ceramics, followed by a heat treatment at 850°C for 10 min. Poling was conducted in an oil bath at 60°C under a DC electric field of 2 kV mm^{-1} for 60 min using a high-voltage polarization system (Huace HV, Beijing Huace Test Instrument, China). The piezoelectric coefficient d_{33} was measured using a quasi-static piezoelectric coefficient tester (HCYD-200, Beijing Huace Test Instrument, China). Dielectric and impedance characteristics were measured with an ultrasonic impedance analyzer (ZX80A, Zhixin Precision Electronics, China). Ferroelectric polarization-electric field (P-E) hysteresis loops were obtained using a ferroelectric analyzer (FE2000, Beijing Huace Test Instrument, China). Compressive strength and stress–strain curves were measured using a universal testing machine (UTM6104, 82 SUNS, China). Surface mechanical properties were characterized via nanoindentation testing (Anton Paar, Graz, Austria). The piezoelectric sensing performance was evaluated using a piezoelectric mechanical force system composed of an electrometer (Keithley 6514), shaker, signal generator, charge amplifier, and data acquisition device.

4.6 | Statistical Analysis

To evaluate the electromechanical performance of the high-solid-loading piezoelectric ceramics, including the sintering shrinkage rate and relative sintered density (Figure 1c,d), d_{33} and ε_r (Figure 2a,c), nanoindentation elastic modulus and hardness, and compressive strength (Figure 3a,b,d), as well as g_{33} and FOM_{off} (Figure 5a), three independent ceramic samples were tested for each case, with the results presented using error bars or error bands. For the sensing performance evaluation (Figures 5c,d,6, and 7), three sensor devices were fabricated and tested, with representative data from one sensor shown in the corresponding figures. Data processing and graphing were performed using Origin. Simulations (Supporting Information) were conducted using COMSOL Multiphysics and nTop. Image data measurements (Figure 4) were performed using ImageJ software with multi-location wall thickness measurements ($n > 5$).

Acknowledgements

This research was supported by the National Natural Science Foundation of China (Grant No. 12272113).

Funding

This work was supported by the National Natural Science Foundation of China (Grant No. 12272113).

Ethics Statement

Informed consent was obtained from the participant (who is also a co-author of this work) for the wearable sensor demonstration and the publication of the related video.

Conflicts of Interest

The authors declare no conflicts of interest.

Data Availability Statement

The data that support the findings of this study are available from the corresponding author upon reasonable request.

16163028, 2026, 79, Downloaded from https://advanced.onlinelibrary.wiley.com/doi/10.1002/adfm.202523909 by Harbin Institute Of Technology, Wiley Online Library on [12/11/2026]. See the Terms and Conditions (https://onlinelibrary.wiley.com/terms-and-conditions) on Wiley Online Library for rules of use; OA articles are governed by the applicable Creative Commons License

References

1. Q. Xu, Y. Tao, Z. Wang, et al., "Highly Flexible, High-Performance, and Stretchable Piezoelectric Sensor Based on a Hierarchical Droplet-Shaped Ceramics With Enhanced Damage Tolerance," *Advanced Materials* 36, no. 18 (2024): 2311624, https://doi.org/10.1002/adma.202311624.

2. T. Xu, W. Wang, X. Bian, et al., "High Resolution Skin-Like Sensor Capable of Sensing and Visualizing Various Sensations and Three Dimensional Shape," *Scientific Reports* 5, no. 1 (2015): 12997, https://doi.org/10.1038/srep12997.

3. Q. Mao, Z. Liao, S. Liu, J. Yuan, and R. Zhu, "An Ultralight, Tiny, Flexible Six-Axis Force/Torque Sensor Enables Dexterous Fingertip Manipulations," *Nature Communications* 16, no. 1 (2025): 5693, https://doi.org/10.1038/s41467-025-60861-8.

4. H. Cui, R. Hensleigh, D. Yao, et al., "Three-Dimensional Printing of Piezoelectric Materials With Designed Anisotropy and Directional Response," *Nature Materials* 18, no. 3 (2019): 234–241, https://doi.org/10.1038/s41563-018-0268-1.

5. Z. Li, X. Yi, J. Yang, L. Bian, Z. Yu, and S. Dong, "Designing Artificial Vibration Modes of Piezoelectric Devices Using Programmable, 3D Ordered Structure With Piezoceramic Strain Units," *Advanced Materials* 34, no. 2 (2022): 2107236, https://doi.org/10.1002/adma.202107236.

6. H. Cui, D. Yao, R. Hensleigh, et al., "Design and Printing of Proprioceptive Three-Dimensional Architected Robotic Metamaterials," *Science* 376, no. 6599 (2022): 1287–1293, https://doi.org/10.1126/science.abn0090.

7. Z. Gao, Y. Lei, Z. Li, et al., "Artificial Piezoelectric Metamaterials," *Progress in Materials Science* 151 (2025): 101434, https://doi.org/10.1016/j.pmatsci.2025.101434.

8. Z. Wang, Y. Meng, S. Tang, et al., "Simultaneous Achievement of Large Electrocaloric Effect and Ultra-Wide Operating Temperature Range in $BaTiO_3$-Based Lead-Free Ceramic," *Journal of Advanced Ceramics* 13, no. 8 (2024): 1234–1241, https://doi.org/10.26599/JAC.2024.9220932.

9. L. Zhao, X. Yuan, X. Zhou, et al., "Three-Dimensional Honeycomb Structured $BaTiO_3$-Based Piezoelectric Ceramics via Texturing and Vat Photopolymerization," *Additive Manufacturing* 95 (2024): 104542, https://doi.org/10.1016/j.addma.2024.104542.

10. A. Chen, J. Su, Y. Li, et al., "3D/4D Printed Bio-Piezoelectric Smart Scaffolds for Next-Generation Bone Tissue Engineering," *International Journal of Extreme Manufacturing* 5, no. 3 (2023): 032007, https://doi.org/10.1088/2631-7990/acd88f.

11. Z. Chen, X. Sun, Y. Shang, et al., "Dense Ceramics With Complex Shape Fabricated by 3D Printing: A Review," *Journal of Advanced Ceramics* 10, no. 2 (2021): 195–218, https://doi.org/10.1007/s40145-020-0444-z.

12. X. Pan, B. Meng, Q. Yang, X. Ping, C. Fang, and Z. Ma, "Dielectric Properties of A and B-Site Doped $BaTiO_3$-Based High-Entropy Ceramics Prepared by Fast Hot-Pressing Sintering," *Ceramics International* 50, no. 3 (2024): 5806–5817, https://doi.org/10.1016/j.ceramint.2023.11.388.

13. C.-L. Liu, Q. Du, C. Zhang, J.-M. Wu, G. Zhang, and Y.-S. Shi, "Fabrication and Properties of $BaTiO_3$ Ceramics via Digital Light Processing for Piezoelectric Energy Harvesters," *Additive Manufacturing* 56 (2022): 102940, https://doi.org/10.1016/j.addma.2022.102940.

14. K. Liu, J. He, T. Li, et al., "Fabrication of Ceramic-Polymer Piezo-Composites With Triply Periodic Minimal Interfaces via Digital Light Processing," *Chinese Journal of Mechanical Engineering: Additive Manufacturing Frontiers* 2, no. 4 (2023): 100104, https://doi.org/10.1016/j.cjmeam.2023.100104.

15. L. Kai, F. Sufeng, W. Xiaoying, and L. Yang, "3D Nanoprinting Piezoceramic With Large Elastic Deformation and High Piezoelectricity," *International Journal of Extreme Manufacturing* 7, no. 4 (2025): 045006, https://doi.org/10.1088/2631-7990/adbe18.

16. Z. Chen, X. Song, L. Lei, et al., "3D Printing of Piezoelectric Element for Energy Focusing and Ultrasonic Sensing," *Nano Energy* 27 (2016): 78–86, https://doi.org/10.1016/j.nanoen.2016.06.048.

17. J. Ye, H. Gong, Y. Zhang, et al., "Piezoelectric Ceramics With Hierarchical Macro- and Micro-Pore Channels for Sensing Applications," *Additive Manufacturing* 79 (2024): 103915, https://doi.org/10.1016/j.addma.2023.103915.

18. H. Lu, H. Cui, G. Lu, et al., "3D Printing and Processing of Miniaturized Transducers With Near-Pristine Piezoelectric Ceramics for Localized Cavitation," *Nature Communications* 14, no. 1 (2023): 2418, https://doi.org/10.1038/s41467-023-37335-w.

19. X. Bai, D. Wang, L. Zhen, et al., "Design and Micromanufacturing Technologies of Focused Piezoelectric Ultrasound Transducers for Biomedical Applications," *International Journal of Extreme Manufacturing* 6, no. 6 (2024): 062001, https://doi.org/10.1088/2631-7990/ad62c6.

20. Z. Liu, X. Hu, R. Bo, et al., "A Three-Dimensionally Architected Electronic Skin Mimicking Human Mechanosensation," *Science* 384, no. 6699 (2024): 987–994, https://doi.org/10.1126/science.adk5556.

21. J. Yang, Z. Li, X. Xin, et al., "Designing Electromechanical Metamaterial With Full Nonzero Piezoelectric Coefficients," *Science Advances* 5, no. 11 (2019): aax1782, https://doi.org/10.1126/sciadv.aax1782.

22. S. Bhandari, G. Vajpayee, L. L. da Silva, M. Hinterstein, G. Franchin, and P. Colombo, "A Review on Additive Manufacturing of Piezoelectric Ceramics: From Feedstock Development to Properties of Sintered Parts," *Materials Science and Engineering: R: Reports* 162 (2025): 100877, https://doi.org/10.1016/j.mser.2024.100877.

23. J. Li, Y. Zhang, M. Yan, et al., "3D Printing of Flexible Piezoelectric Composite With Integrated Sensing and Actuation Applications," *Advanced Powder Materials* 3, no. 5 (2024): 100226, https://doi.org/10.1016/j.apmate.2024.100226.

24. C. Chen, X. Wang, Y. Wang, et al., "Additive Manufacturing of Piezoelectric Materials," *Advanced Functional Materials* 30, no. 52 (2020): 2005141, https://doi.org/10.1002/adfm.202005141.

25. S. Chen, R. Wang, H. Li, et al., "High-Precision $BaTiO_3$ Piezoelectric Ceramics via Vat Photopolymerization 3D Printing," *Journal of the European Ceramic Society* 44, no. 14 (2024): 116706, https://doi.org/10.1016/j.jeurceramsoc.2024.116706.

26. S. A. Rasaki, D. Xiong, S. Xiong, F. Su, M. Idrees, and Z. Chen, "Photopolymerization-Based Additive Manufacturing of Ceramics: A Systematic Review," *Journal of Advanced Ceramics* 10, no. 3 (2021): 442–471, https://doi.org/10.1007/s40145-021-0468-z.

27. Y. Yang, Z. Chen, X. Song, et al., "Three Dimensional Printing of High Dielectric Capacitor Using Projection Based Stereolithography Method," *Nano Energy* 22 (2016): 414–421, https://doi.org/10.1016/j.nanoen.2016.02.045.

28. H. Chen, B. Chen, J. Li, H. Yan, Y. Zeng, and J. Chen, "Optimization of Vat-Polymerization Binder Formulation for 3D Printing Ceramic Slurry Using D-Optimal Mixture Experimental Design," *Composites Part B: Engineering* 260 (2023): 110777, https://doi.org/10.1016/j.compositesb.2023.110777.

29. Z. Cheng, L. Chen, Y. Liao, et al., "The Effect of Solid Content on the Anisotropy for 3D Printed Barium Titanate Piezoelectric Ceramics," *Ceramics International* 50, no. 23 (2024): 50697–50703, https://doi.org/10.1016/j.ceramint.2024.09.414.

30. M. J.-H. Reavley, H. Guo, J. Yuan, et al., "Ultrafast High-Temperature Sintering of Barium Titanate Ceramics With Colossal Dielectric Constants," *Journal of the European Ceramic Society* 42, no. 12 (2022): 4934–4943, https://doi.org/10.1016/j.jeurceramsoc.2022.04.056.

31. X. An, Y. Mu, J. Chen, et al., "Compositional Optimization of High-Solid-Loading Ceramic Cores via 3D Printing," *Additive Manufacturing* 58 (2022): 103054, https://doi.org/10.1016/j.addma.2022.103054.

32. C. Sun, J. Chen, S. Yan, D. Jiang, X. Chu, and S. Yuan, "Piezoelectric-Pneumatic Micro-Jet Printing of High Viscous Piezoelectric Slurry," *Additive Manufacturing* 66 (2023): 103469, https://doi.org/10.1016/j.addma.2023.103469.

16163028, 2026, 79, Downloaded from https://advanced.onlinelibrary.wiley.com/doi/10.1002/adfm.202523909 by Harbin Institute Of Technology, Wiley Online Library on [12/11/2026]. See the Terms and Conditions (https://onlinelibrary.wiley.com/terms-and-conditions) on Wiley Online Library for rules of use; OA articles are governed by the applicable Creative Commons License

33. K. Liu, C. Zhou, J. Hu, et al., "Fabrication of Barium Titanate Ceramics via Digital Light Processing 3D Printing by Using High Refractive Index Monomer," *Journal of the European Ceramic Society* 41, no. 12 (2021): 5909–5917, https://doi.org/10.1016/j.jeurceramsoc.2021.04.044.

34. S. Liu, W. Wang, W. Xu, et al., "Continuous Three-Dimensional Printing of Architected Piezoelectric Sensors in Minutes," *Research* 2022 (2022): 9790307, https://doi.org/10.34133/2022/9790307.

35. Z. Jiang, L. Cheng, Y. Zeng, et al., "3D Printing of Porous Scaffolds $BaTiO_3$ Piezoelectric Ceramics and Regulation of Their Mechanical and Electrical Properties," *Ceramics International* 48, no. 5 (2022): 6477–6487, https://doi.org/10.1016/j.ceramint.2021.11.192.

36. X. Chen, J. Sun, B. Guo, et al., "Effect of the Particle Size on the Performance of $BaTiO_3$ Piezoelectric Ceramics Produced by Additive Manufacturing," *Ceramics International* 48, no. 1 (2022): 1285–1292, https://doi.org/10.1016/j.ceramint.2021.09.213.

37. K. Liu, J. Hu, Y. Du, et al., "Influence of Particle Size on 3D-Printed Piezoelectric Ceramics via Digital Light Processing With Furnace Sintering," *International Journal of Applied Ceramic Technology* 19, no. 5 (2022): 2461–2471, https://doi.org/10.1111/ijac.14074.

38. K. Liu, Y. Sun, H. Sun, et al., "Effect of Particle Grading on the Properties of Photosensitive Slurry and $BaTiO_3$ Piezoelectric Ceramic via Digital Light Processing 3D Printing," *Journal of the European Ceramic Society* 43, no. 8 (2023): 3266–3274, https://doi.org/10.1016/j.jeurceramsoc.2023.02.021.

39. Z. Jiang, Y. Sun, J. Chen, and Y. Zeng, "Control of Electromechanical Performance in 3D Printing Lattice-Structured $BaTiO_3$ Piezoelectric Ceramics," *Journal of Advanced Ceramics* 13, no. 7 (2024): 987–1001, https://doi.org/10.26599/JAC.2024.9220912.

40. Y. Chen, X. Bao, C.-M. Wong, et al., "PZT Ceramics Fabricated Based on Stereolithography for an Ultrasound Transducer Array Application," *Ceramics International* 44, no. 18 (2018): 22725–22730, https://doi.org/10.1016/j.ceramint.2018.09.055.

41. J. Cheng, Y. Chen, J.-W. Wu, X.-R. Ji, and S.-H. Wu, "3D Printing of $BaTiO_3$ Piezoelectric Ceramics for a Focused Ultrasonic Array," *Sensors* 19, no. 19 (2019): 4078, https://doi.org/10.3390/s19194078.

42. Z. Wang, X. Yuan, J. Yang, et al., "3D-Printed Flexible, Ag-Coated PNN-PZT Ceramic-Polymer Grid-Composite for Electromechanical Energy Conversion," *Nano Energy* 73 (2020): 104737, https://doi.org/10.1016/j.nanoen.2020.104737.

43. X. Liu, J. Liu, L. He, Y. Shang, and C. Zhang, "3D Printed Piezoelectric-Regulable Cells With Customized Electromechanical Response Distribution for Intelligent Sensing," *Advanced Functional Materials* 32, no. 26 (2022): 2201274, https://doi.org/10.1002/adfm.202201274.

44. C. Jiang, Y. Li, H. Yin, et al., "Multiscale Interconnected and Anisotropic Morphology Genetic Piezoceramic Skeleton Based Flexible Self-Powered 3D Force Sensor," *Advanced Functional Materials* 35, no. 38 (2025): 2503120, https://doi.org/10.1002/adfm.202503120.

45. P. Zhou, Z. Zheng, B. Wang, and Y. Guo, "Self-Powered Flexible Piezoelectric Sensors Based On Self-Assembled 10 nm $BaTiO_3$ Nanocubes On Glass Fiber Fabric," *Nano Energy* 99 (2022): 107400, https://doi.org/10.1016/j.nanoen.2022.107400.

46. L. S. Gi, Y. Ki Jun, W. Sang Min, and Y. Jae-Young, "Advanced Approaches to Decoupled Sensory Signal Monitoring in Human Interface Systems," *International Journal of Extreme Manufacturing* 7, no. 4 (2025): 042003, https://doi.org/10.1088/2631-7990/adbc4e.

47. X. Song, Z. Chen, L. Lei, K. Shung, Q. Zhou, and Y. Chen, "Piezoelectric Component Fabrication Using Projection-Based Stereolithography of Barium Titanate Ceramic Suspensions," *Rapid Prototyping Journal* 23, no. 1 (2017): 44–53, https://doi.org/10.1108/RPJ-11-2015-0162.

48. W. Wang, J. Sun, B. Guo, X. Chen, K. P. Ananth, and J. Bai, "Fabrication of Piezoelectric Nano-Ceramics via Stereolithography of Low Viscous and Non-Aqueous Suspensions," *Journal of the European Ceramic Society* 40, no. 3 (2020): 682–688, https://doi.org/10.1016/j.jeurceramsoc.2019.10.033.

49. A. Smirnov, S. Chugunov, A. Kholodkova, et al., "The Fabrication and Characterization of $BaTiO_3$ Piezoceramics Using SLA 3D Printing at 465 nm Wavelength," *Materials* 15, no. 3 (2022): 960, https://doi.org/10.3390/ma15030960.

50. L. A. Chavez, B. R. Wilburn, P. Ibave, et al., "Fabrication and Characterization of 3D Printing Induced Orthotropic Functional Ceramics," *Smart Materials and Structures* 28, no. 12 (2019): 125007, https://doi.org/10.1088/1361-665X/ab4e0a.

51. H. Kim, A. Renteria-Marquez, M. D. Islam, et al., "Fabrication of Bulk Piezoelectric and Dielectric $BaTiO_3$ Ceramics Using Paste Extrusion 3D Printing Technique," *Journal of the American Ceramic Society* 102, no. 6 (2019): 3685–3694, https://doi.org/10.1111/jace.16242.

52. A. Renteria, J. A. Diaz, B. He, et al., "Particle Size Influence on Material Properties of $BaTiO_3$ Ceramics Fabricated Using Freeze-Form Extrusion 3D Printing," *Materials Research Express* 6 (2019): 115211, https://doi.org/10.1088/2053-1591/ab4a36.

53. J. Li, N. Li, Y. Zheng, et al., "Interfacially Locked Metal Aerogel Inside Porous Polymer Composite for Sensitive and Durable Flexible Piezoresistive Sensors," *Advanced Science* 9, no. 23 (2022): 2201912, https://doi.org/10.1002/advs.202201912.

54. Y. Wang, H. Wu, L. Xu, H. Zhang, Y. Yang, and Z. L. Wang, "Hierarchically Patterned Self-Powered Sensors for Multifunctional Tactile Sensing," *Science Advances* 6, no. 34 (2020): abb9083, https://doi.org/10.1126/sciadv.abb9083.

55. Z. Zhao, J. Tang, J. Yuan, et al., "Large-Scale Integrated Flexible Tactile Sensor Array for Sensitive Smart Robotic Touch," *ACS Nano* 16, no. 10 (2022): 16784–16795, https://doi.org/10.1021/acsnano.2c06432.

56. J.-H. Lee, E. Kim, H. Zhang, et al., "Rational Design of All Resistive Multifunctional Sensors With Stimulus Discriminability," *Advanced Functional Materials* 32, no. 1 (2022): 2107570, https://doi.org/10.1002/adfm.202107570.

57. T. Sun, H. Zhao, J. Zhang, et al., "Degradable Bioinspired Hypersensitive Strain Sensor With High Mechanical Strength Using a Basalt Fiber as a Reinforced Layer," *ACS Applied Materials & Interfaces* 14, no. 37 (2022): 42723–42733, https://doi.org/10.1021/acsami.2c12479.

58. X. Chen, F. Wang, L. Shu, et al., "A Single-Material-Printed, Low-Cost Design for a Carbon-Based Fabric Strain Sensor," *Materials & Design* 221 (2022): 110926, https://doi.org/10.1016/j.matdes.2022.110926.

59. Y. Zhang, J. Yang, X. Hou, et al., "Highly Stable Flexible Pressure Sensors With a Quasi-Homogeneous Composition and Interlinked Interfaces," *Nature Communications* 13, no. 1 (2022): 1317, https://doi.org/10.1038/s41467-022-29093-y.

60. P. Lu, L. Wang, P. Zhu, et al., "Iontronic Pressure Sensor With High Sensitivity and Linear Response Over a Wide Pressure Range Based on Soft Micropillared Electrodes," *Science Bulletin* 66, no. 11 (2021): 1091–1100, https://doi.org/10.1016/j.scib.2021.02.019.

61. Z. Ding, W. Li, W. Wang, et al., "Highly Sensitive Iontronic Pressure Sensor With Side-by-Side Package Based on Alveoli and Arch Structure," *Advanced Science* 11, no. 24 (2024): 2309407, https://doi.org/10.1002/advs.202309407.

62. S. Chen, Y. Wang, L. Yang, F. Karouta, and K. Sun, "Electron-Induced Perpendicular Graphene Sheets Embedded Porous Carbon Film for Flexible Touch Sensors," *Nano-Micro Letters* 12, no. 1 (2020): 136, https://doi.org/10.1007/s40820-020-00480-8.

63. N. Li, L. Liu, Y. Liu, and J. Leng, "Metamaterial-Based Electronic Skin With Conformality and Multisensory Integration," *Advanced Functional Materials* 34, no. 49 (2024): 2406789, https://doi.org/10.1002/adfm.202406789.

64. Y. Zhang, M. Tang, C. Chen, Y. Shi, W. Wang, and Z. Wu, "Realization of Precise Human Gesture Recognition via a Self-Powered Flexible Sensor Based on Thermal Expansion-Treated and Potassium Ion-Modified VMT/PDMS Film," *Advanced Functional Materials* 35, no. 52 (2025): 10616, https://doi.org/10.1002/adfm.202510616.

16163028, 2026, 79, Downloaded from https://advanced.onlinelibrary.wiley.com/doi/10.1002/adfm.202523909 by Harbin Institute Of Technology, Wiley Online Library on [12/11/2026]. See the Terms and Conditions (https://onlinelibrary.wiley.com/terms-and-conditions) on Wiley Online Library for rules of use; OA articles are governed by the applicable Creative Commons License

65. C. Chen, S. Zhao, C. Pan, et al., "A Method for Quantitatively Separating the Piezoelectric Component From the As-Received "Piezoelectric" Signal," *Nature Communications* 13, no. 1 (2022): 1391, https://doi.org/10.1038/s41467-022-29087-w.

66. J. Su, Z. Niu, Y. Hu, et al., "Superelastic Triboelectric Aerogel Enabled by Cross-Scale Fibers and Heterojunction Particles for Wearable Intelligent Neck Guard," *Advanced Functional Materials* 36, no. 5 (2026): 15065, https://doi.org/10.1002/adfm.202515065.

67. P. Wang, Y. Sun, X. Lan, Y. Liu, and J. Leng, "Material-Process Controlled DLP Printing of $BaTiO_3$ With Synchronized Precision and Piezoelectricity for Micro-Transducers," *Ceramics International* 52, no. 6 (2026): 8122–8132, https://doi.org/10.1016/j.ceramint.2026.01.020.

Supporting Information

Additional supporting information can be found online in the Supporting Information section.

Supporting File 1: adfm77062-sup-0001-SuppMat.docx.

Supporting File 2: adfm77062-sup-0002-VideoS1.mp4.

Supporting File 3: adfm77062-sup-0003-VideoS2.mp4.

16163028, 2026, 79, Downloaded from https://advanced.onlinelibrary.wiley.com/doi/10.1002/adfm.202523909 by Harbin Institute Of Technology, Wiley Online Library on [12/11/2026]. See the Terms and Conditions (https://onlinelibrary.wiley.com/terms-and-conditions) on Wiley Online Library for rules of use; OA articles are governed by the applicable Creative Commons License